Modeling of an Electromechanical Valve Actuator for a Camless Engine[1]

Yan Wang, Anna Stefanopoulou
University of California, Santa Barbara, CA
Mohammad Haghgooie, Ilya Kolmanovsky, Mazen Hammoud
Ford Motor Company, Dearborn, MI

Abstract

Automotive engines equipped with camless valvetrains (so called camless engines) have been studied for over twenty years, but production vehicles with engines of this type are still not available due to difficulties in ensuring adequate and reliable valve performance in this valvetrain. For an electromechanical camless valvetrain, the actuator noise caused by high contact velocities of the moving parts of the actuator has been identified as a key problem. With the idea of providing tools to address this problem, in this paper we develop a physics-based model for an electromechanical camless valve actuator. The model parameters are identified using appropriately constructed steady-state and transient experiments, and good agreement between the model and the experimental transient response trajectories is demonstrated. Finally, a sensitivity study is performed to characterize the ability of the control signal to affect the reduction of the contact velocities.

1 Introduction

Conventional internal combustion engines use mechanically driven camshafts to actuate intake and exhaust valves. While this system is convenient and reliable, the fixed timing of the valve events with respect to the piston motion is typically selected as a compromise among fuel economy, emissions, maximum torque output, and valvetrain noise, vibration and harshness (NVH).

The growing need to improve fuel economy and reduce emissions led to the introduction of an alternative valvetrain technology, namely, a camless valvetrain. In the camless valvetrain, the valve motion is controlled directly by a valve actuator, without mechanical linkage to the camshaft. As a result, the timing of the exhaust and intake valve opening and closing can be optimized for each engine operating condition. Various studies have shown that a camless valvetrain can alleviate many otherwise necessary engine design tradeoffs by supplying extra degrees of freedom to the overall powertrain system (Ahmad and Theobald, 1989; Gray, 1988; Ma, 1986; Meacham, 1970; Schechter and Levin, 1998). Specifically, it has been shown that controlling the intake valve events can eliminate the need for throttled operation in gasoline engines, thereby reducing pumping losses and improving fuel economy (Ashhab et al., 1998; Elrod and Nelson, 1986; Miller el al., 1997). Other benefits of camless engines include higher maximum torque output, which is optimized for different driving conditions, cylinder de-activation, and elimination of external exhaust gas recirculation, etc. (Schechter and Levin, 1998).

While VVT can be obtained using a wide spectrum of different technologies (see a review of various VVT technologies in Schechter and Levin, 1998), the highest degree of flexibility and the fastest VVT capability is achieved in truly camless engines with either electrohydraulic (Kim, et al., 1997) or electromechanical (Butzmann et al., 2000) actuators. These camless actuator technologies are under intensive development by several manufacturers, with the electromechanical technology currently considered by many to be in a relatively more developed stage. The issues that have to be addressed in the actuator design include cost, reliability, packaging, power consumption, noise and vibrations. The noise has been identified as the main problem with the electromechanical actuator technology. It may, in fact, preclude the usage of such systems, if satisfactory solutions are not found.

The noise in an electromechanical actuator is caused by high contact velocities of the moving parts of the actuator. The noise can be reduced if the contact velocities are reduced, i.e., the so called *soft-landing* is achieved. In a conventional valvetrain the valve profiles are carefully optimized to reduce the noise and the optimal solution is mechanically embedded into the valvetrain design during manufacturing of the camshaft lobes. In a camless valvetrain it is the responsibility of the control system to ensure the adequate actuator performance at varying engine operating conditions. To facilitate the analysis and controller design for an ElectroMechanical Camless Valvetrain (EMCV), an actuator model is developed and validated in this paper.

The paper is organized as follows. First, we de-

[1] Corresponding author, e-mail: anna@engineering.ucsb.edu.
Research supported in part by the National Science Foundation under contract NSF ECS-97-33293; matching funds were provided by FORD MO. CO.

scribe a physics-based model for the EMCV. The model represents the mechanical, electrical and magnetic subsystems of the actuator and their interactions. To identify the model parameters and the nonlinear characteristics of the actuator, special experiments have been developed and implemented both on the engine with EMCV in the dynamometer and with the actuator alone on a bench-top. Unlike in the work (Butzmann et al., 2000), here we take a special care to ensure model validity even at small gap distances between the armature and the coil, which is exactly the region where high contact velocities responsible for noise production tend to occur. A close agreement between the model and measured actuator responses is demonstrated. Finally, the results of a sensitivity study are reported whereby numerical simulations of the model are used to characterize the ability of a control system to reduce the contact velocity as well as to affect the actuator response time.

2 System Overview

Figure 1 shows the EMCV actuator with a valve at three typical positions. There are two magnets (upper and lower magnets), two springs (actuator and valve springs) and an armature in the actuator. The two magnets are coils wound on ferromagnetic material. The coils are driven by currents generated by electronics. The electronics are driven by a pulse-width modulated voltage and the duty cycle of this voltage signal determines the steady-state current value. When the coil is activated, a magnetic field is generated and consequently the magnetic force is applied on the armature in the magnetic field. The two springs are adjusted such that both are always compressed for any position of the armature in between the two magnets. The armature is subjected to the magnetic force and actuator spring force and passes the forces to the valve. The actuator uses the spring force to accelerate the masses (the actuator spring bolt, the armature, the valve, and the valve spring bolt), then uses the electromagnetic force to attract and dwell the valve and the armature.

The equilibrium of the spring-mass system is at the

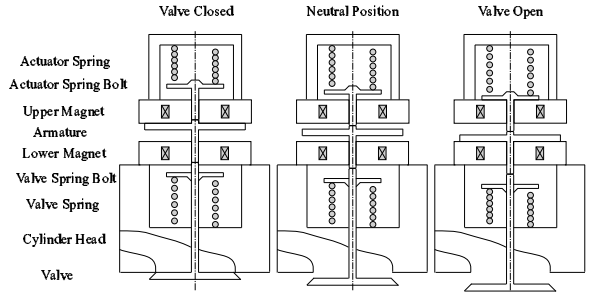

Figure 1: EMCV actuator with a valve

middle position between the two magnets. Therefore, when there is no current on coils, the valve will stay in the middle position ("Neutral Position" in Figure 1). When the valve is closed ("Valve Closed" in Figure 1), there is a voltage applied on the upper coil which generates a holding current. The holding current depends on the spring force and the pressure difference between the cylinder and the exhaust/intake manifold. If the valve is scheduled to open at t_0, the voltage applied to the upper coil should be regulated to zero at $t_0 - \tau_m$; the time τ_m is necessary for the discharge of the magnetic field. Then a voltage with high duty cycle, d_c, is applied to the lower coil at t_1. A magnetic field is generated that attracts the armature to contact the lower coil and maintains the maximum valve lift. The current generated by this high voltage, d_c, is denoted as catching current. Once the contact is ensured and quasi-static conditions of the mechanical subsystem are reached, the voltage applied to the lower coil can be reduced. The time that the lower duty cycle voltage, d_h, is applied to the lower coil is denoted by t_2. By controlling t_2 we affect the power consumption of the electrical subsystem. When the valve is closing, the operation is similar with the voltage applied on the lower coil regulated to zero at t_3. In the Figure 2, we

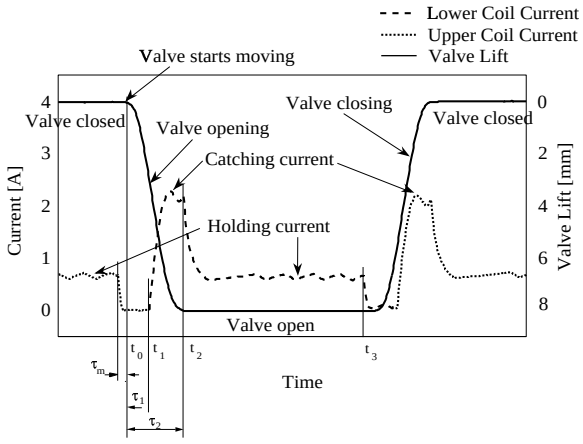

Figure 2: The driving current of the EMCV actuator and the corresponding valve profile

define the time intervals $\tau_1 = t_1 - t_0$ and $\tau_2 = t_2 - t_0$ that are used in the sensitivity analysis section.

To summarize, the actuator consists of electrical, magnetic and mechanical subsystems, which are interconnected with each other (shown in Figure 3). The variables and the three subsystems will be explained in more detail in the next sections. Because of the symmetry, we only analyze the subsystems when the valve is opening.

3 Electrical Subsystem

Figure 4 shows the electrical subsystem of the actuator. The equation of the electrical circuit is:

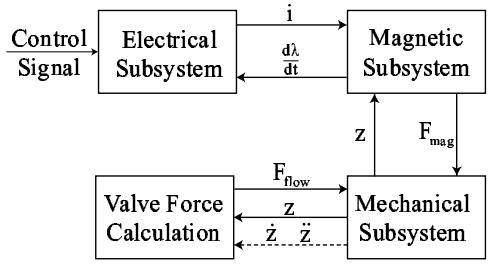

Figure 3: The interaction of subsystems of the EMCV

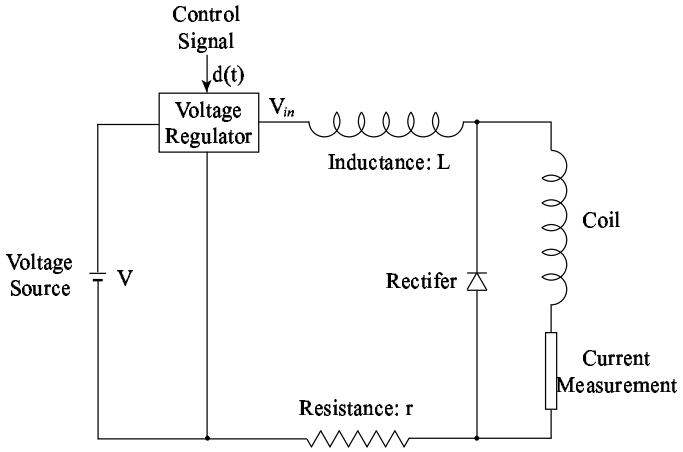

Figure 4: The electrical subsystem of the EMCV

$$V_{in} = L\frac{di}{dt} + r \cdot i + \frac{d\lambda}{dt}, \tag{1}$$

where,

- V_{in} is the effective voltage on the power electronics, determined by the control signal $d(t)$, $(V_{in} = V_{in}(d(t)) = d(t) \cdot V)$,
- L is the external inductance of the electronics circuit,
- i is the current in the coil,
- r is the resistance in the electronics circuit,
- λ is the flux linkage in the magnetic field generated by the coil.

V, L and r are constants and λ is a nonlinear function.

The control signal $d(t)$ is the duty cycle command to the electronics, $d(t) \in [0, 1]$. If we consider the operation we described for valve opening (Figure 2), we have the following $d(t)$ for the lower coil in one operation cycle:

$$d(t) = \begin{cases} 0 & \text{when } t < t_1 \\ d_c & \text{when } t_1 \leq t < t_2 \\ d_h & \text{when } t_2 \leq t < t_3 \\ 0 & \text{when } t > t_3. \end{cases} \tag{2}$$

4 Mechanical Subsystem

Figure 5 shows the mechanical subsystem and the associated free-body diagram when the valve is at the middle position. The moving mass of the mechanical system includes three parts: the upper spring bolt, the armature, and the valve with the valve spring bolt. In this paper, we lump all the three pieces in one mass because they are moving together during most of the travel from one coil to another. Figure 5 shows the spring forces from the actuator spring (F_{us})and the valve spring (F_{ls}) and the magnetic force (F_{mag}). Also shown are the damping force inside the actuator (F_{damp}) and the gas flow force (F_{flow}) on the valve.

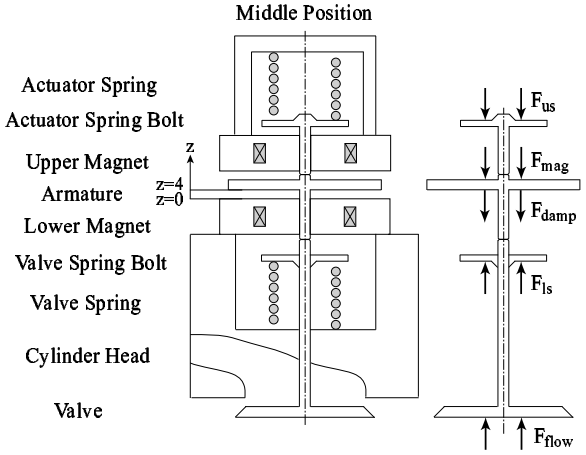

Figure 5: The mechanical subsystem of the EMCV

The differential equation describing the one mass, spring mechanical subsystem is given by Newton's Law,

$$m\ddot{z} = -F_{mag} - F_{us} + F_{ls} - F_{damp} + F_{flow}, \tag{3}$$

where,

- m is the mass of the moving parts in the actuator,
- z is the distance between the armature and the lower coil, $z \in [0, 8]$ mm, when $z = 0$, the armature contacts the lower coil and the valve is in the open position, when $z = 8$ mm, the armature contacts the upper coil and the valve is in the closed position,

F_{mag} is the magnetic force generated by the coil,

F_{us} is the spring force from the upper spring,

F_{ls} is the spring force from the lower spring,

F_{damp} is the damping force inside the actuator due to the friction,

F_{flow} is the gas flow force on the valve generated when the valve separates two chambers with different pressures.

The positive direction for the forces is in the direction of increasing distance z.

In the calculation of the spring force F_{us} and F_{ls}, we assume linear springs. This assumption was tested by measuring the spring force for different spring compression. From the measurement, the spring constant was identified as $k_s = 75N/mm$ for both springs. Therefore, we have the following spring forces:

$$F_{us} = k_s(z_s + z - 4) = k_s(z - 4) + k_s z_s$$
$$F_{ls} = k_s(z_s + 4 - z) = k_s(4 - z) + k_s z_s,$$

where, z_s is the initial compression of both the springs at the equilibrium point ($z = 4\ mm$). Consequently, we have $F_{ls} - F_{us} = 2 \cdot k_s(4 - z)$. Here we notice that if we want to satisfy the requirement that both springs are compressed during the whole travel of the armature (F_{ls} and F_{us} are both positive when $z \in [0, 8]\ mm$), it's required that $z_s > 4\ mm$.

Figure 6 shows an experimental trace of the distance z and an estimate of the exhaust valve gas flow force based on the upstream (P_{cyl}) and the downstream (P_{exh}) pressure with equation $F_{flow} = (P_{cyl} - P_{exh})S_{ev}$, where S_{ev} is the area of the exhaust valve. When the valve starts opening, there is no magnetic force on the armature since the currents on both coils are regulated to zero and the spring force magnitude is $|2k_s(4 - 8)| = 600\ N$. It is shown that $|F_{flow}| < 40\ N$ during valve opening is small compared to the spring force. It should be noted that, when the engine operates at higher loads, this force may become significant. Here, we assume that F_{flow} is an unknown external force applied to the mechanical subsystem.

The damping force is $F_{damp} = k_b\dot{z}$, where k_b is the damping ratio. Finally, we obtain the dynamics for the mechanical subsystem in the form:

$$m\ddot{z} = -F_{mag} + 2 \cdot k_s(4 - z) - k_b\dot{z} + F_{flow}. \quad (4)$$

5 Magnetic Subsystem

Figure 7 shows the magnetic circuit (the dash line loop) of the lower coil and the armature in the actuator.

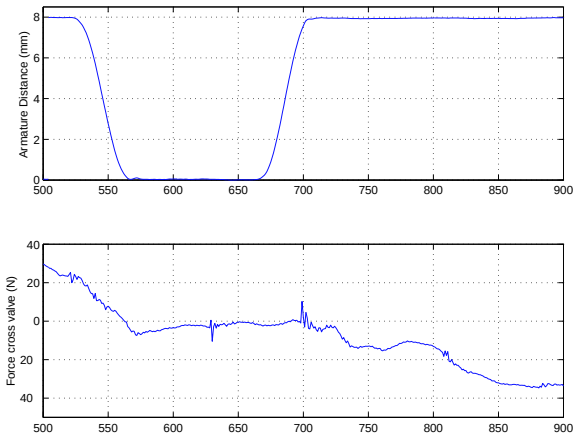

Figure 6: Approximation of the gas flow force across the exhaust valve for low load conditions

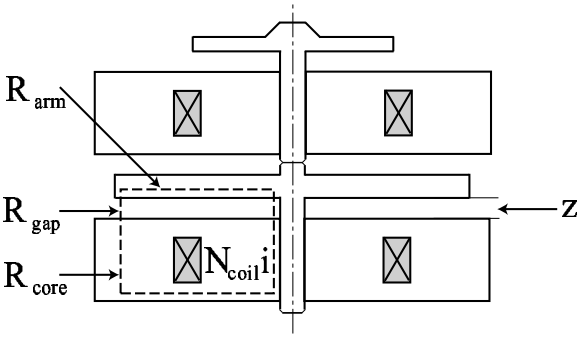

Figure 7: The magnetic subsystem of the EMCV

The equation of the magnetic circuit is given by (Sadiku, 1994):

$$N_{coil} \cdot i = \frac{\lambda}{N_{coil}}(\Re_{core} + \Re_{arm} + \Re_{gap}), \quad (5)$$

where, N_{coil} is the number of turns of the coil, and $\Re_{core}$, $\Re_{arm}$, and $\Re_{gap}$ are the reluctance of the core material, the armature, and the air gap, respectively. The reluctances $\Re_{core}$, $\Re_{arm}$, and $\Re_{gap}$ are calculated by (Sadiku, 1994);

$$\Re = \frac{\ell}{\mu S},$$

where

ℓ is the mean length of the circuit loop,

S is the cross-section area of the magnetic material,

μ is the permeability.

Therefore, $\Re_{core} = \frac{C_1}{\mu_{core}(z,i)} = \Re_{core}(z, i)$ with a constant $C_1 = \frac{\ell_{core}}{S_{core}}$, because ℓ_{core} and S_{core} are constants determined by the dimension of the actuator,

and $\mu_{core} = \mu_{core}(z,i)$ is a function of both z and i which is determined by the nonlinear property of this core material. $\Re_{gap} = C_2 z = \Re_{gap}(z)$ with a constant $C_2 = \frac{1}{\mu_0 S_{gap}}$, because ℓ_{gap} is the gap length z, S_{gap} is a constant determined by the dimension of the actuator, and μ_{gap} is the permeability of free space μ_0. $\Re_{arm} = C_3$ is a constant since ℓ_{arm}, S_{arm}, and μ_{arm} are constants determined by the dimension and property of the armature. Then (5) can be written as:

$$N_{coil} \cdot i = \frac{\lambda}{N_{coil}}\left(\frac{C_1}{\mu_{core}(z,i)} + C_2 z + C_3\right) \quad \Rightarrow$$

$$\lambda = \frac{N_{coil}^2 \cdot i}{\frac{C_1}{\mu_{core}(z,i)} + C_2 z + C_3} = \lambda(z,i). \tag{6}$$

Thus λ is a nonlinear function of the armature distance (z) and the current (i), and requires careful characterization in order to obtain an accurate estimation of the magnetic force.

Equation (1) shows that λ affects the electrical subsystem. At the same time, λ is related with the magnetic force (F_{mag}). The magnetic force generated by this magnetic field is calculated from the co-energy, W',

$$F_{mag} = \frac{\partial W'}{\partial z} \quad \text{where} \quad W' = \int_0^i \lambda di. \tag{7}$$

Since the variables i and z are independent, (7) becomes:

$$F_{mag} = \int_0^i \frac{\partial \lambda}{\partial z} di \quad \Rightarrow \quad \frac{\partial F_{mag}}{\partial i} = \frac{\partial \lambda}{\partial z}. \tag{8}$$

Because $\lambda = \lambda(z,i)$, we know:

$$\frac{\partial F_{mag}}{\partial i}(z,i) = \frac{\partial \lambda}{\partial z}(z,i). \tag{9}$$

6 Parameter Identification

The nonlinear functions of $\lambda(z,i)$ in (6) and $F_{mag}(z,i)$ in (7) depend on the magnetic property of the ferromagnetic material. To find these unknown nonlinear functions, steady-state and dynamic experiments have been conducted. Dynamic experiments were performed by operating an experimental engine equipped with this EMCV actuator in a dynamometer. Bench-top experiments with a stand-alone actuator were conducted to complete the steady-state actuator characterization. These steady-state experiments give us pairs of current and distance and the corresponding magnetic force. To guide our derivation of the relation among them, we used the physical relation detailed in (Cheung et al., 1993).

The relation between flux linkage (λ) and current can be split into two regions: a linear region (when $\lambda \leq \lambda_s$, the flux depends linearly on the current) and a saturation region (when $\lambda \geq \lambda_s$, the rate of change of flux with respect to the current decreases for increasing value of i). Figure 8 shows the theoretical relation between λ and i for different values of z that is given by:

$$\lambda(z,i) = \left(\frac{k_1}{k_2 + z} - k_3\right) \cdot i \quad \text{when } \lambda(z,i) \leq \lambda_s,$$

$$(\lambda(z,i) - \lambda_0(z))^2 = \frac{k_4(i - i_0(z))}{(k_5 + z)^2}, \quad \text{when } \lambda(z,i) \geq \lambda_s,$$

where, λ_s is a constant, while $\lambda_0(z)$ and $i_0(z)$ are chosen such that C^1 continuity of the function of $\lambda(z,i)$ is preserved.

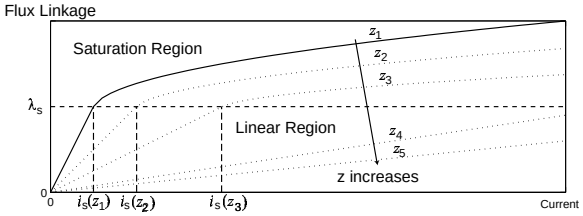

Figure 8: Relation between λ and i

From the steady-state data, it is shown (Figure 9) that, for a fixed distance z, $\frac{\partial^2 F_{mag}}{\partial i^2} > 0$ for small values of i ($i < i_s$). For large currents ($i \geq i_s$), $\frac{\partial^2 F_{mag}}{\partial i^2} < 0$. By inspection of the steady-state data, we determined the current and the associated distance where the rate of change of F_{mag} with respect to i starts to decrease and denote the current as $i_s(z)$, where,

$$i_s(z) = k_6 + k_7 z. \tag{10}$$

Using (9), in the linear region, we have:

$$F_{mag}^{Lin}(z,i) = \frac{k_1}{2(k_2 + z)^2} i^2. \tag{11}$$

We know that (11) can be rewritten in the form:

$$\frac{\sqrt{F_{mag}^{Lin}(z,i)}}{i}(k_2 + z) = \frac{1}{\sqrt{2}}\sqrt{k}_1, \tag{12}$$

thus, $\sqrt{k}_1$ and k_2 can be obtained by linear regression of steady-state data that satisfy $i \leq i_s(z)$.

For the F_{mag} in the saturation region, an approach is to use a polynomial (13), in which all the coefficients $\alpha's$ are determined from steady-state data which satisfy

$i \geq i_s(z)$,

$$\begin{aligned} F_{mag}^{Sat}(z,i) &= \alpha_0 + \alpha_1\sqrt{i} + \alpha_2 i + \alpha_3 i^2 \\ &+\alpha_4(0.01+z) + \alpha_5\frac{1}{0.01+z} \\ &+\alpha_6 i(0.01+z) + \alpha_7\frac{i}{0.01+z} \\ &+\alpha_8\sqrt{i}(0.01+z) + \alpha_9\frac{\sqrt{i}}{0.01+z} \end{aligned} \tag{13}$$

Thus we have the following expression for F_{mag}:

$$F_{mag}(z,i) = \begin{cases} F_{mag}^{Lin}(z,i) & \text{when } i \leq i_s(z) \\ F_{mag}^{Sat}(z,i) & \text{when } i \geq i_s(z). \end{cases} \tag{14}$$

Here we made some modification to the calculation of $F_{mag}^{Sat}(z,i)$ to assure the continuity of $F_{mag}(z,i)$, i.e., $F_{mag}^{Sat}(z,i_s(z)) = F_{mag}^{Lin}(z,i_s(z))$. Figure 9 shows the estimation (solid lines) using (14) and measurement ($*$) of F_{mag}. The regression matches the data well.

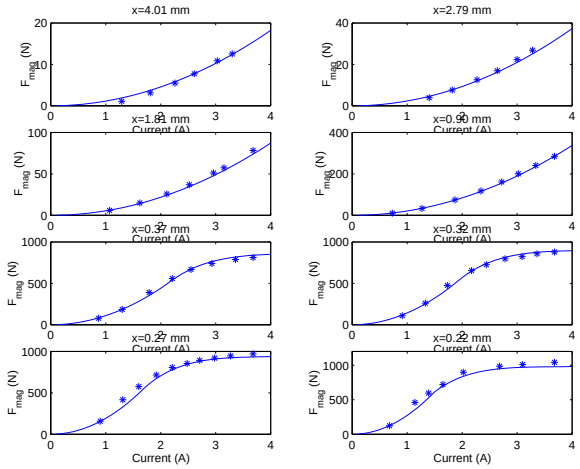

Figure 9: The regression result for $F_{mag}(i,z)$ at several distances

Once $F_{mag}(z,i)$ is known, $\frac{\partial F_{mag}}{\partial i}(z,i)$ can be determined. Let $\chi_1(z,i) \stackrel{\text{def}}{=} \frac{\partial \lambda}{\partial z}(z,i) = \frac{\partial F_{mag}}{\partial i}(z,i)$ defined by (14). At the same time, we know that:

$$\begin{aligned} \frac{d\lambda(z,i)}{dt} &= \frac{\partial\lambda(z,i)}{\partial z}\frac{dz}{dt} + \frac{\partial\lambda(z,i)}{\partial i}\frac{di}{dt}, \quad \textit{and} \\ \frac{d\lambda(z,i)}{dt} &= V_{in} - r\cdot i - L\frac{di}{dt}, \end{aligned} \tag{15}$$

then, we define the new function χ_2 as:

$$\chi_2(z,i) \stackrel{\text{def}}{=} L + \frac{\partial\lambda(z,i)}{\partial i} = \frac{V_{in} - r\cdot i - \chi_1(z,i)\frac{dz}{dt}}{\frac{di}{dt}}, \tag{16}$$

and $\chi_2(z,i)$ can be regressed by dynamic data which includes V_{in}, i, and z, and $\frac{di}{dt}$ and $\frac{dz}{dt}$ that are derived by the numerical calculation from i and z, respectively.

Finally, the differential equations are given by:

$$\begin{aligned} \frac{di}{dt} &= \frac{V_{in} - r\cdot i - \chi_1(z,i)v}{\chi_2(z,i)} \\ \frac{dz}{dt} &= v \\ \frac{dv}{dt} &= \frac{1}{m}(-F_{mag}(z,i) + 2\cdot k_s(4-z) - k_b v), \end{aligned} \tag{17}$$

where, $\chi_1(z,i)$, $\chi_2(z,i)$, and $F_{mag}(z,i)$ are now known static nonlinearities and k_s, k_b and r are known fixed constants.

There is one thing to be noticed in (17). To avoid singularity, $\chi_2(z,i)$ can not be zero in the operating range. This is guaranteed by the physics. Figure 8 shows that $\frac{\partial\lambda(z,i)}{\partial i}$ should be positive, which means that $\chi_2(z,i) > 0$ for all $i > 0$ and $z > 0$.

7 Model Validation

In this section, we perform simulations by numerically implementing the differential equations (17) in simulink using s-function. Simulation result are compared with the dynamical experimental data collected from an operating engine equipped with an EMCV.

Figures 10 and 11 show the comparison of simulation results and the dynamic data for two different driving conditions, 1500 RPM, 4 bar, and 2500 RPM, 5.5 bar. It is seen that the discrepancy in the predicted current and position responses from the actual dynamic measurements is not significant while the difference in the velocity traces is significant for small z. The experimental data show the smooth change of velocity when z is close to 0, but the simulation shows an acceleration followed by a large contact velocity.

The relation between F_{mag} and z shows that the acceleration before contact predicted by the model is reasonable. Specifically, as z is reduced, F_{mag} becomes larger than the spring force when z is small (as shown in Figure 12). The same acceleration has been documented by Butzmann, et al, 2000.

A possible explanation for the difference between the model and the experimental data is that the measurement of the position is not fast enough and the resolution is not high, and consequently the numerical approximation of the velocity is not accurate. Measurements from a sensor with higher resolution and wider bandwidth do, in fact, show this acceleration. An additional reason for the modeling error may be as follows. Note first that our model is based on the assumption that the three parts in the actuator move together all the time. Assume there is a distance (z_g) between the armature and the actuator spring bolt when

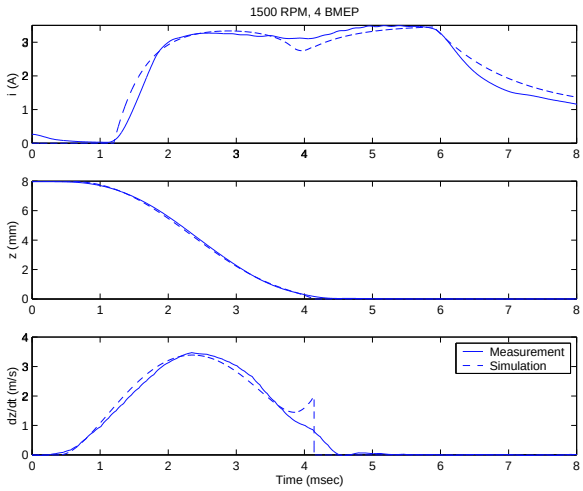

Figure 10: Comparison of the simulation result and the transient measurement at 1500 RPM, 4 bar

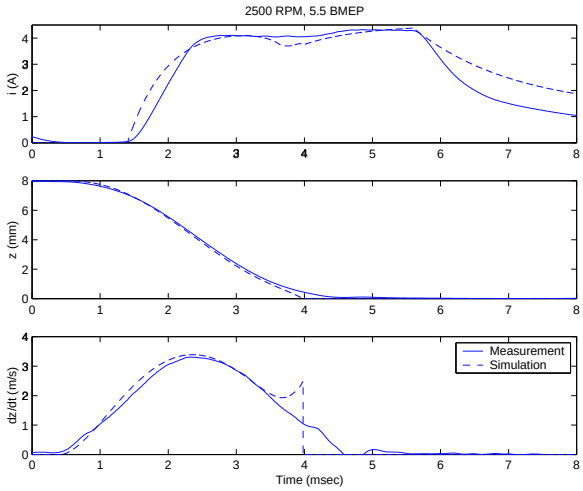

Figure 11: Comparison of the simulation result and the transient measurement at 2500 RPM, 5.5 bar

the armature contacts the lower coil and the actuator spring bolt contacts the upper coil. Then if we consider the opening of the valve, the spring force on the three body is $F_{ls} - F_{us} = 2 \cdot k_s(4 - z)$ before the two parts separate, while the spring force on the armature is $F_{ls} = k_s(z_s + 4 - z)$ after the separation. Because $z_s > 4\ mm$, the spring force on the armature after separation is larger than before separation. Then if the actuator spring bolt and the armature separate near the start of the acceleration shown in Figure 10 and 11, the actuator spring bolt contact velocity is actually the value when they separate, while the armature will be accelerated by a smaller acceleration if the initial compression of the spring is well-tuned (because the spring force is larger). Consequently, the contact velocity of both the armature and the actuator spring bolt can potentially be smaller than the one predicted by our model (shown in Figure 10 and Figure 11).

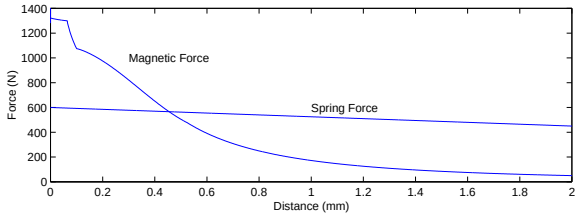

Figure 12: Magnetic and spring forces vs. distance

8 Sensitivity Analysis

Even though we can try to improve the prediction of the model by including the three pieces in the armature and valve assembly, we judge that the validity of the model is sufficient for control analysis and design purposes. In this section, we look into the effect of the control signal $d(t)$ on the contact velocity and the relative authority of its parameters in lowering the contact velocity.

The valve motion is mostly determined by the spring and a damper, except that it is also affected by a magnetic force when the valve is close to the magnet. Figure 13 shows the valve position when it's a free oscillation, a damped oscillation, and a damped oscillation with a magnetic force corresponding to a constant catching current. If the armature moves without any damping and with zero magnetic force, it is a free oscillation and it will start from the upper magnet ($z = 8\ mm$) and reach the lower magnet ($z = 0\ mm$) with zero velocity in 3.6 $msec$, followed by going back to the upper magnet. If the damping is significant, the armature can't reach the lower magnet (the dash line in Figure 13) because the damper will dissipate energy. However, the electrical subsystem will add energy to the actuator through the magnetic force. If the addition of energy from the electronics is more than the dissipation from the damper, the armature will reach the lower magnet (the dotted line in Figure 13) with a nonzero

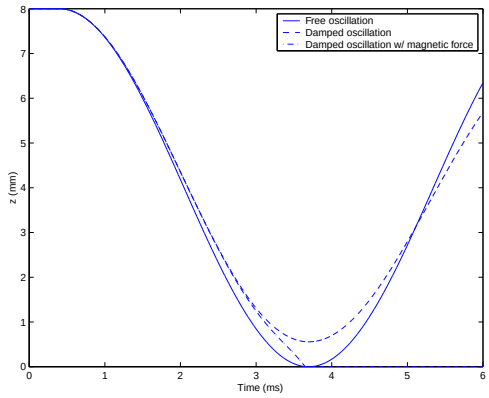

Figure 13: Different valve trajectories in different conditions

velocity in around 3.6 $msec$. In this case, the kinetic energy of the moving masses is the subtraction of the dissipated energy (denoted as E_b) from the electronics energy (denoted as E_V), and consequently the contact velocity is $v_c = \sqrt{\frac{2(E_V - E_b)}{m}}$, where $E_b = \int_{t_0}^{T_c} k_b \cdot dv(t)$, and $E_V(t) = \int_{t_1}^{T_c} F_{mag}(t) \cdot dz(t)$, in which T_c is the time when the valve moves to its maximum lift. It's then clear that v_c is related to $v(t)$, $z(t)$, T_c, and $F_{mag}(t)$, which are determined by the control signal $d(t)$. The following plots show the change of the contact velocity as well as the landing time when $d(t)$ is changed.

Figure 14 shows that increasing τ_1 will decrease contact velocity while increase travel time. It is also found from the simulation that when τ_1 is too large, catching can not be achieved.

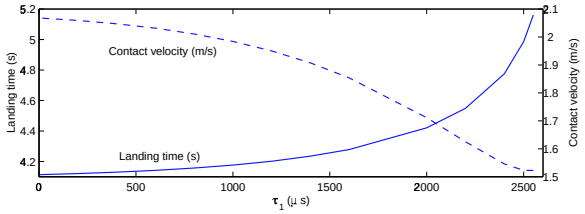

Figure 14: Contact velocity and travel time vs. τ_1

Figure 15 shows that reduction of duty cycle d_c will decrease contact velocity while increase travel time. If d_c is too small, catching can not be achieved.

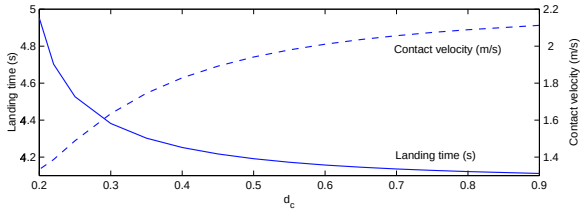

Figure 15: Contact velocity and travel time vs. catching duty cycle (d_c)

Figure 16 shows that when τ_2 is less than some value, decreasing τ_2 will decrease contact velocity while the travel time doesn't change much.

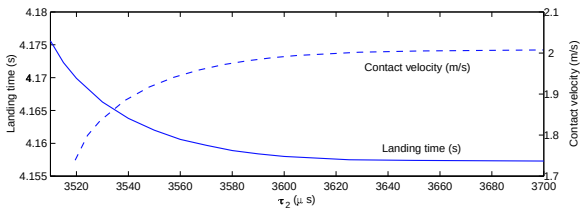

Figure 16: Contact velocity and travel time vs. τ_2

Figures 14 to 16 show that τ_1, d_c, and τ_2 can change the contact velocity. Hence, it is feasible to develop a control algorithm that can adjust them to reduce the contact velocity.

9 Conclusion

In this paper, we developed an EMCV actuator model. The model parameters were identified by steady-state and dynamic experiments. Then we validated the model by comparing the simulation with the actual measurements. Finally we reported the result of the sensitivity analysis that sheds light in the future control design direction.

10 Acknowledgement

Thanks to Rob Otterspeer and Alexander Stotsky from Volvo, Jeff Cook from Ford Motor Company, and Garrick McNey and Adam Matthews from UCSB, for their help and advice.

References

1. Ahmad T. and Theobald M. A., "A Survey of Variable Valve Actuation Technology," SAE Paper No. 891674.

2. Ashhab M. S., Stefanopoulou A. G., Cook J. A., and Levin M., "Camless Engine Control for Robust Unthrottled Operation," SAE Paper No. 981031.

3. Butzmann S., Melbert J., and Koch A., "Snesorless Control of Electromagnetic Actuators for Variable Valve Train," SAE Paper No. 2000-01-1225

4. Cheung N.C., Lim K.W., Rahman M.F., "Modeling a Linear and Limited Travel Solenoid" Proceedings of the IECON '93, p.1567-72.

5. Elrod A. C. and Nelson M. T., "Development of a Variable Valve Timing Engine to Eliminate the Pumping Losses Associated with Throttled Operation," SAE Paper No. 860537.

6. Gray C., "A Review of Variable Engine Valve Timing," SAE Paper No. 880386.

7. Kim D., Anderson M, Tsao T.-C., and Levin M., "A Dynamic Model of a Springless Electrohydraulic Camless Valvetrain System," SAE Paper, No. 970248.

8. Ma T. H., 1986, "Recent Advances in Variable Valve Timing," *Alternative and Advanced Automotive Engines,* Plenum Press, 1986.

9. Meacham G.-B., "Variable Cam Timing as an Emission Control Tool," SAE Paper No. 700645.

10. Miller R. H., Davis G. C., Newman C. E., and Levin M. B., "Unthrottled Camless Valvetrain Strategy for Spark-Ignited Engines," Proceedings of the 19th Annual Fall Technical Conference of the ASME Internal Combustion Engine Design Division, *Advanced Engine Design*, ed. T. Uzkan, ICE-Vol. 29-1, pp.81-94, 1997.

11. Sadiku M.N.O., "Elements of Electromagnetics" 2^{nd} ed., Oxford University Press, p. 382-3

12. Schechter M. M. and Levin M. B., "Camless Engine," SAE Paper No. 960581, 1996.